

A Novel Classification Method of Neural Response to Mechanosensory Stimuli in the Honey Bee Antennal Lobe

Jiakun Li^{1,2}, Ross Iaci¹, Katherine Wei³, Hong Lei³, and Mainak Patel¹

¹Department of Mathematics, William & Mary, Williamsburg, VA 23187-8795, USA

²Division of Biostatistics & Health Data Science, University of Minnesota, Minneapolis, MN 55414, USA

³School of Life Sciences, Arizona State University, Tempe, AZ 85281, USA

Abstract

While the antennal lobe (AL) has primarily been studied from the perspective of encoding olfactory information, some reports in the literature show that AL neurons respond not only to chemosensory input, but also to mechanosensory input in the form of wind buffeting the antennae. However, the detailed nature of mechanosensory responses to wind speed, and the functional role of such input within the AL, remain, in large part, to be elucidated. In this combined experimental and analytical work, spiking activity from AL neurons in response to unscented air puffs delivered at various speeds is recorded and analyzed to extract trends in response patterns to mechanosensory input. We begin by aggregating data over all wind speeds and using the time-averaged firing rate over either the peri-stimulus or post-stimulus period to cluster neuronal responses within each of these temporal epochs. This methodology, however, allows for neither a fine discrimination among response patterns nor an assessment of changes in a neuron’s response pattern across wind speeds; hence, we then cluster neuronal response curves, employing a metric termed the Hausdorff distance to measure the differences between neuronal responses over the conjoined peri- and post-stimulus epochs, on a wind speed by wind speed basis. We find widespread mechanosensory responses among AL neurons that cluster into several categories, and, strikingly, observe that the response type of an individual neuron can shift with changes in wind speed.

1 Introduction

The olfactory sense in insects serves to not only identify, parse, and classify ambient odors, but also to guide the tracking of an odor source. The former task requires only chemosensory detection; the binding of airborne odorant molecules to an array of specialized sensors on the antennae - each of which detects a specific molecular motif - relays sufficient information to the antennal lobe (AL), via the antennal nerve (AN) for odor identification to occur [12],[34],[35],[16],[1],[38],[21],[24],[25],[23].

The latter task, however, is complicated by air turbulence - turbulent air flow tends to produce complex patterns of ‘choppy’ odor strands of varying sizes and concentrations interspersed with clear air, rarely resulting in a straightforward concentration gradient that the animal can follow to the odor source [33],[5],[20]. Thus, odor stimulation during mid-flight tracking occurs in pulsatile fashion; odor pulses tend to increase in spatial frequency and concentration as the odor source is approached [33],[5],[20],[19], and in order to successfully track the origin of an odor stimulus the insect must be able to resolve the spatiotemporal dynamics of the odor plume (in addition to performing odor identification); resolving spatiotemporal plume dynamics, however, requires integration of mechanosensory input (reflecting wind speed information) with olfactory input [17][31][32][22].

In accordance with the importance of mechanosensory input to olfactory navigation, integration of these two streams of information has been observed across species and beginning early in the olfactory pathway, including bimodal sensilla on the antennae [11],[27],[14],[39] and mechanosensory responses in the first olfactory processing center [13],[9],[40],[4],[10],[2],[3],[37],[6],[31],[22],[30], termed the AL in insects or OB (olfactory bulb) in mammals. While responses to purely mechanosensory input within the AL have been reported in the literature, a quantification of the nature, variety, and wind speed-dependence of such responses has not been performed - such an analysis is a prerequisite to understanding the functional dynamics of chemosensory and mechanosensory integration within the AL.

In this combined experimental and statistical work, we present electrophysiological data on the responses of honeybee AL neurons to unscented air puffs (pure mechanosensory input) while systematically varying wind speed. Our data suggest that mechanosensory responses are widespread within the AL, and that response profiles can qualitatively vary from neuron to neuron and even across wind speeds for a single neuron. We then develop and present a clustering methodology, and we show that this methodology is capable of grouping neurons by response profile, which in turn allows assessment of the dependence of response profile on wind speed. This serves as a proof-of-concept, showing that this methodology can provide an automated way to classify neuronal response types in more expansive data sets. The rest of the paper is organized as follows: In section 1.1 we describe the data collection process. In section 1.2 we illustrate how the data is preprocessed. In section 2, we apply clustering methods to the neuronal response data, in the form of time-averaged firing rates, aggregated across all wind speeds. In section 3 we introduce the Hausdorff distance as a measure of dissimilarity between individual neuronal response profiles and incorporate it with agglomerative clustering to perform clustering of neuronal response curves for individual wind speeds. We conclude with a discussion of the methods and analyses and potential further directions.

1.1 Experimental procedures

Honey bees (*Apis mellifera* Ligustica), commonly known as Italian bees, were maintained by the Bee Facility of Arizona State University. The hives were placed on a balcony, exposing them to a natural day-night cycle. Non-pollen foragers were collected each day for electrophysiological recordings.

Multichannel extracellular recording methods [15, 29] were used to measure responses of the AL.

Bees were cold-anaesthetized before being harnessed on a custom-made Plexiglass block. The bee head and antennae were immobilized on the block with low-melting-temperature utility wax. A rectangular window was cut open between the two compound eyes and between the ocelli and the base of the two antennae. The glandular material and some trachea membrane were removed to expose the two ALs. The bee was positioned on a recording stage in such a way that the anterior side of the brain was facing upward.

A constant saline flow was introduced into the head capsule to ensure the brain tissue was immersed in an adequate ionic environment. A standard bee saline recipe was adopted from literature [7], which contains 130 mM NaCl, 6 mM KCl, 4 mM MgCl₂ x 6H₂O, 5 mM CaCl₂ x 2H₂O, 160 mM Sucrose, 25 mM D-Glucose x H₂O, 10 mM HEPES. The pH was adjusted to 6.7 and the final osmolarity was 500 mOsm. A reference electrode, made of a thin silver wire, was placed behind the brain in the saline water.

A Tucker-Davis Technologies (TDT) RZ2 microprocessor system, in conjunction with a PZ2 preamplifier from the same manufacturer (TDT®, Alachua, FL 32615 USA) was used to digitize neural signals, which was sampled with a Neuronexus A2x2 multichannel probe (Neuronexus®, Ann Arbor, MI 48108 USA), as described in [15]. Briefly, the probe was carefully inserted into the central neuropil of the AL aided with a Leica micromanipulator. After initial contact, the probe was slowly moved deeper, a few microns each step, until spikes appeared. Care was taken to insert probes approximately in the same location each time. The acquisition software was configured to acquire the spike waveforms at 25 kHz sampling rate, and the 16 recording channels were grouped in the software to form 4 tetrodes [8], facilitating the separation of units in later analysis.

To quantify the neural responses, the tetrode waveforms were exported from the TDT acquisition software to the Offline Sorter® program (Plexon® Inc., Dallas, TX USA), which allows automatic as well as manual sorting of the waveforms. In Offline Sorter®, each set of tetrode waveforms, composed of 32 (A/D points) x 4 (recording sites) thus 128 dimensions, was reduced to 3 dimensions using principal component analysis, and each concatenated waveform was projected onto a 3D space consisting of the first three principal components for visualization. In general, *k*-means automatic sorting or semi-automatic sorting using templates was first applied, then visual inspection and adjustment were taken to yield multiple units from each tetrode. The time stamps of all waveforms were then exported to a spike analysis program, Neuroexplorer® (Nex Technologies, Dallas, TX USA) or Matlab® (Mathworks, Natick, MA USA), for further analysis. Units are treated as individual neurons in the antennal lobe.

1.2 Data preprocessing

Using a Gilmont flow meter, wind pulses of 500 millisecond (ms) durations at five different speeds (30, 60, 90, 120, 150 milliliters per second) were delivered to honeybee subjects and the electrophysiological recordings were performed on 32 AL neurons, with five trials per stimulus. The resulting five recordings are averaged in each of the binned intervals, described next, to generate one observed spike count per bin for each of the $n = 32$ individual neurons over the entire recording epoch.

The spike-sorted responses of individual AL neurons during the 500ms wind pulse period are binned into 50ms windows. For example, neurons with binned responses are shown in Figure 1, with the time interval between the two dotted red lines defining the stimulation period, the region to the left measuring the background activity during the pre-stimulus period, and to the right of the second red line measuring neuron spike activity in the post-stimulus period. Note that, in order to account for the variation in background activity, the average firing rate during the pre-stimulus period, the first 1000ms, is subtracted from each binned spike-sorted response over the entire measured period. The neuron in the top left panel of Figure 1 is labeled a *post-stimulus* responder due to the increased spike activity after the stimulus period, the neuron in the top right panel is termed a *regular* responder because of the high spike activity immediately following stimulus onset, the bottom left panel is an example of a neuron termed a *delayed* responder since the highest spike activity is observed in the middle of the stimulus period, and finally, the bottom right panel is an example of a neuron that did not have a marked increase in neural response over the entire epoch and is termed a *non-responder*. Note that the regular and delayed responders are later grouped together and referred to as *peri-stimulus* responders, and non-responders subsumed into the *low* responder group.

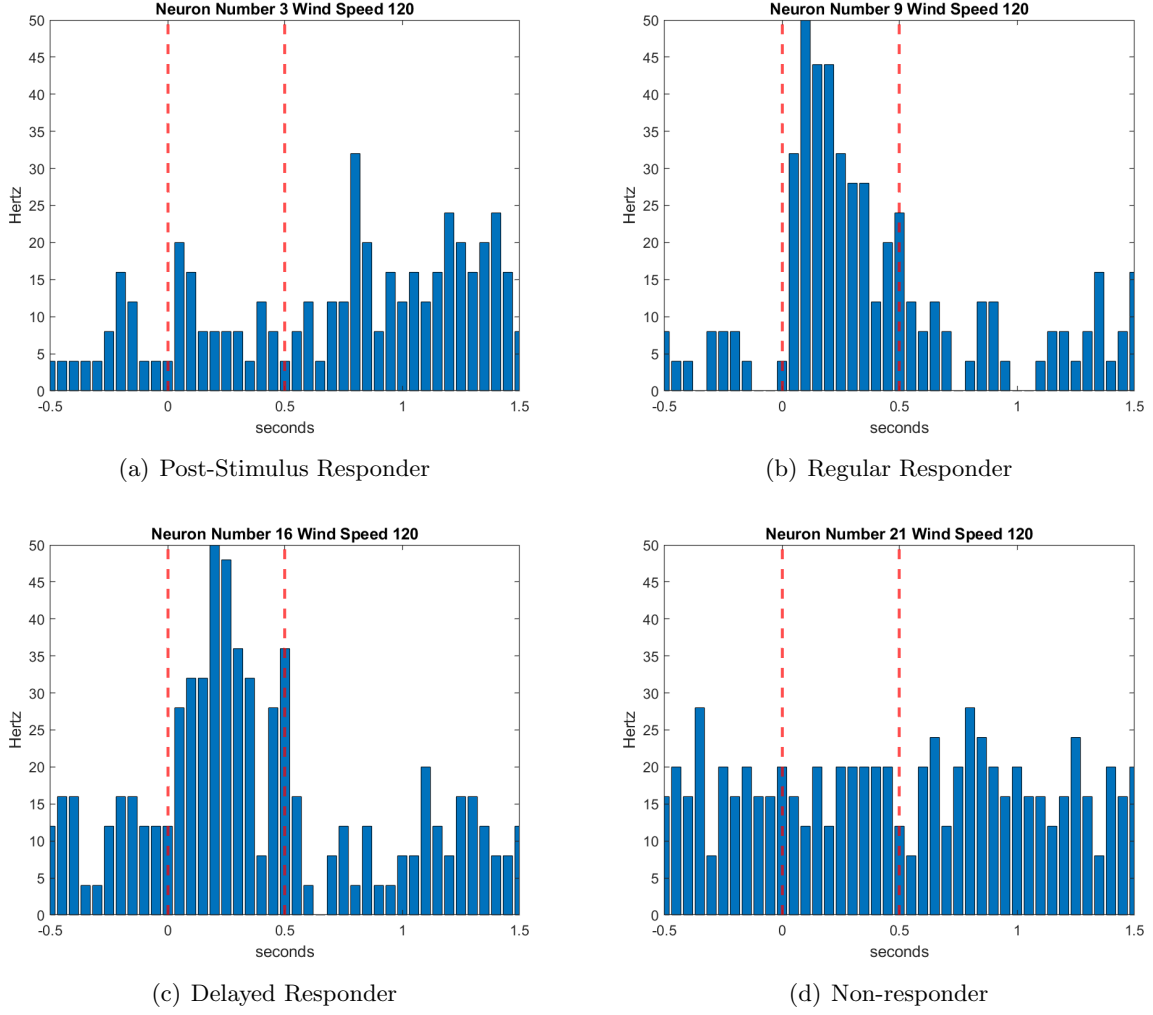


Figure 1: Bar plots of neurons exhibiting different responding patterns. The y-axis is the firing rate measured in hertz, and the x-axis is time in seconds. The two dotted red lines represent the onset and offset of stimulus. 1(a), 1(b), 1(c) corresponds respectively to a strong post-stimulus responder, a regular responder, and a delayed responder. 1(d) is a non-responder which exhibits activity no different than background during the stimulus.

2 Aggregate wind speed analysis

2.1 Introduction

From the binned data and bar plots in Figure 1, we observe that the neurons exhibit different response patterns. To quantify the neural response, the data is segmented by taking the average firing rate over two specific intervals: (i) (peri) the entire duration of the stimulus (500ms) and (ii) (post) 1000ms immediately following stimulus offset. We constructed a data set for the firing rates for both intervals, with $n = 32$ individual observations corresponding to an individual neuron and the firing rate at each of the $p = 5$ wind speed levels.

In Section 2.2 a k -means cluster analysis is performed using the $k++$ means algorithm to determine the different types of neuronal response patterns. In our analysis, we adjusted for individual variation by subtracting background activity, and since measurement units and variability were similar across variables, we did not transform to the z -scale. In Section 2.3, since the dimension is $p > 3$, a Principal Component Analysis (PCA) is performed on the data to visually characterize the differences between the clusters in lower dimensions. In Section 2.4, again to visualize the difference between groups, a Canonical Variate Analysis (CVA) is performed where the data is projected into lower dimensional subspaces that maximize the between-cluster variability relative to the within-cluster variation.

2.2 K-means clustering

To identify groups of similarly responding neurons, a k -means clustering analysis is performed using the k -means++ algorithm with $k = 3$ centroids. The squared Euclidean distance between the centroids of each group, or the L_1 distance, often termed the “city block” distance, is used in the k -means procedure implemented in MATLAB. The centroid method was chosen since, like the “nearest neighbor” and “group average” methods, this leads to “spherical” clusters exhibiting high internal affinity, Krzanowski (2001). This method is also suggested by MacQueen (1967).

The number of clusters was chosen using a k -elbow plot of the distortion score as shown in Figure 2. Specifically, for a fixed number of centroids k , or equivalently a fixed number of clusters, the distortion score is calculated as the total sum of the squared distances of each point to the centroid of its assigned cluster. The score is then plotted against a range of values $k \ll n$ and the optimal number of centroids is determined visually by finding the point on the curve where the differences between successive distortion scores becomes negligible.

The k -means++ algorithm proceeds as follows:

- (1) Select an observation at random from the data set and define this value as the first centroid, denoted as c_1 .
- (2) Compute the distances from each observation to c_1 and denote the distance between c_1 and any observation x_m , $m \in \{1, 2, \dots, n\}$, as $d(x_m, c_1)$.
- (3) Select another observation as the next centroid c_2 from the remaining $n - 1$ observations where each observation has the probability of being selected, denoted p_m ,

$$p_m = \frac{d^2(x_m, c_1)}{\sum_{j=1}^n d^2(x_j, c_1)}.$$

Repeat steps (2) – (3) until the k centroids have been determined. Next, the k -means algorithm is applied to the remaining $n - k$ observations to determine the k clusters with centers $\{c_1, c_2, \dots, c_k\}$.

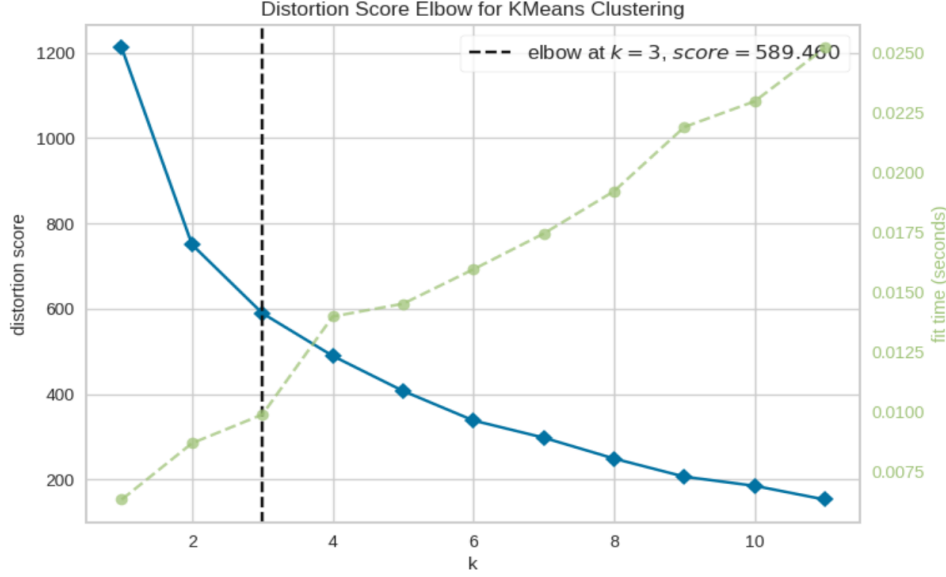


Figure 2: An elbow plot for the k -means clustering to determine the optimal number of clusters.

2.3 Principal Component Analysis

Figure 3 shows the clusters visualized using Principal Component Analysis (PCA). The variances explained by the first two principal components are shown in Table 2. The numbers shown in Figure 3 represent neurons numbered ordinally from the data. These numbers are “identifiers” that allow for the tracking of the neurons in each cluster at different wind speeds. Figure 3(a) shows the plot of the first two principal components (PCs) for the data corresponding to the peri-stimulus interval, with each neuron’s cluster identification colored red, blue or green. The neurons are grouped into $k = 3$ distinct clusters, where the optimal number of clusters is determined based on the elbow plot in Figure 2. Notably, neurons 9, 10 and 11 of the blue cluster form the most separated and distinct group, with the firing rate histograms showing that these neurons exhibit strong peri-stimulus responses in the three highest wind speeds and are therefore classified as peri-stimulus responders.

Table 1 gives the loadings for the first two principal components, with the first PC explaining nearly 80% of the variance. For the peri-stimulus period, the loadings for the first PC are an unequal weighted average with the highest weights on winds speeds 120 and 150; as a result, this is termed the “high wind speed” coefficient vector. Figure 3 shows that, for both the peri-stimulus (Figure 3(a)) and post-stimulus (Figure 3(b)) intervals, the first PC segments neurons into three categories: low, medium and high responders.

Within the peri-stimulus period (Figure 3(a)), neurons with high firing rates for windspeeds 120 and 150 produce the highest PC score and are indicated as the blue cluster in the figure, and termed *high responders*. Neurons with moderate PC scores indicate a lower response and form a second cluster, labeled green, and are referred to as *moderate responders*. The final cluster, depicted in red, are neurons with a low response in the peri-stimulus period and termed *low responders*. However, neuron 32 appears borderline, since its assignment shifted between the moderate and high

responder clusters depending on the initial centroids generated in the k -means++ algorithm. The classification of neuron 32 is further investigated in Section 2.4.

Figures 3(b) shows the clustering results for the post-stimulus interval. Similar to the peri-stimulus period, the analysis produced three clusters, with the most distinct group on the far right of the plot, again corresponding to larger first PC scores. For the original data, the group consists of four neurons: 1, 3, 4 and 32. Figure 3(b) shows that these neurons exhibit post-stimulus responses in the three highest wind speeds and therefore, are classified as *post-stimulus high responders*.

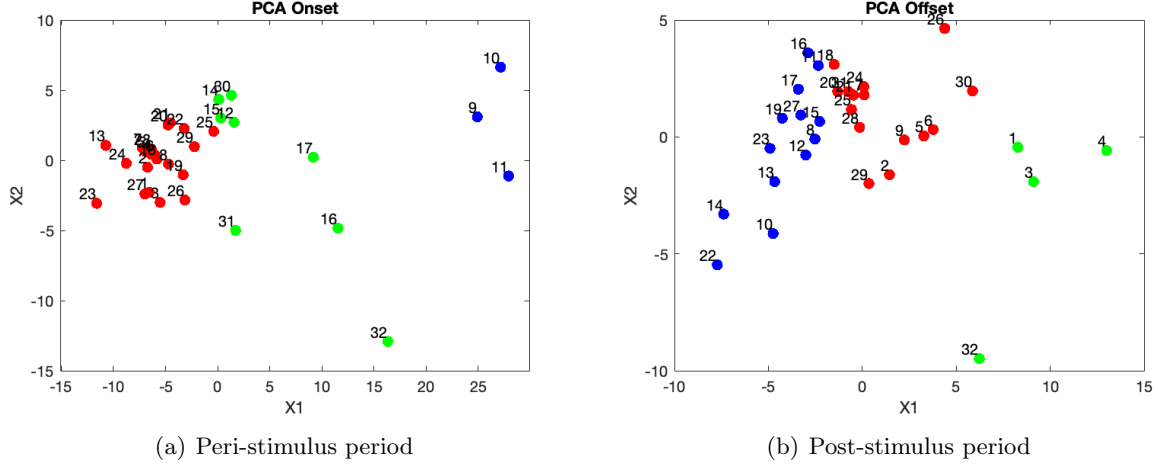


Figure 3: Plots of the k -means clustering results for the peri-stimulus and the post-stimulus intervals, visualized in two dimensions using PCA - first PC (x -axis) vs second PC (y -axis).

PCA Results Section 2.3 -Principal Component Loadings		
	<u>1st PC</u>	<u>2ndPC</u>
Peri-stimulus	(0.0066, 0.0836, 0.2732 , 0.8530 , 0.4367)	(0.4495, 0.1360, -0.0536, -0.4014, 0.7845)
Post-stimulus	(0.1121, 0.1214, 0.6094 , 0.7486 , 0.2024)	(0.4689, 0.1323, 0.6366, -0.5413, -0.2536)

Table 1: Loadings for the first two principal components.

PCA Results Section 2.3 - % of Variance Explained		
	<u>1st PC</u>	<u>2nd PC</u>
Peri-stimulus	79.40%	8.97%
Post-stimulus	52.59%	18.34%

Table 2: Percentage of variance explained by the first two principal components.

2.3.1 Rotated Principal Components

Since the previous analysis determined that the first two PCs explain most of the variance ($> 88\%$) in the peri-stimulus period, and a large percentage ($> 70\%$) in the post-stimulus period, the interpretation of the two dimensional subspace defined by the first two principal component coefficient vectors is key to unveiling the windspeeds that best differentiate response patterns. Rotations of the axes within this two dimensional subspace can simplify the interpretation of the PCs (Jolliffe, (2002)), and can be used to support the interpretations of the PCA results in the previous section - note that, the total amount of variance explained in the rotated subspace remains unchanged. To this end, we consider the well-known Varimax orthogonal rotation criterion (Abdi, 2003), which rotates the first two PCs by maximizing the sum of the variances of the squared loadings with the goal of pushing as many of the components of the PC coefficient vector towards zero as possible, and the remaining closer to 1 or -1 .

Table 3 gives the first two rotated PC coefficient vectors. For the peri-stimulus response, windspeeds 120 and 150 primarily dominate the rotated first PC, and for the post-stimulus response, windspeeds 120 and 90 have the largest influence. This is consistent with the results in Section 2.3, with the rotation simplifying the interpretation of the PC loadings: for the peri-stimulus response, the first principal component loads most heavily on wind speed 120, while the second principal component primarily loads on wind speed 150; for the post-stimulus response, the first and second PCs weigh primarily on wind speeds 120 and 90, respectively.

Rotated PC Section 2.3.1 - Rotated Principal Component Loadings				
	<u>1st PC</u>		<u>2nd PC</u>	
Peri-stimulus	(-0.1492, 0.0314, 0.2748, 0.9392 , 0.1384)		(0.4240, 0.1565, 0.0442, -0.0816, 0.8872)	
Post-stimulus	(-0.2197, 0.0063, 0.0492, 0.9207 , 0.3187)		(0.4292, 0.1795, 0.8799 , 0.0753, -0.0611)	

Table 3: Loadings for the first two PCs after Varimax rotation.

2.4 Canonical Variate Analysis

In this section, we consider another latent variable technique, Canonical Variate Analysis (CVA), to visualize the key differences between the neuronal responses. CVA considers the group structure determined in the k -means clustering analysis by projecting the segmented data into subspaces that maximize the separation between groups. Different from PCA, CVA depends on the segmentation of the data.

Specifically, CVA determines the projections of the data into one-dimensional subspaces that maximize the variability between clusters relative to the within-cluster variability. The within-group

covariance matrix \mathbf{W} and the between-group variance matrix \mathbf{B} are defined as

$$\mathbf{W} = \frac{1}{(n-k)} \sum_{i=1}^k \sum_{j=1}^{n_i} (\mathbf{x}_{ij} - \bar{\mathbf{x}}_i)(\mathbf{x}_{ij} - \bar{\mathbf{x}}_i)^\top \quad \text{and} \quad \mathbf{B} = \frac{1}{(k-1)} \sum_{i=1}^k n_i (\bar{\mathbf{x}}_i - \bar{\mathbf{x}})(\bar{\mathbf{x}}_i - \bar{\mathbf{x}})^\top.$$

The first eigenvector \mathbf{e}_1 of the scatter matrix of $\mathbf{W}^{-1}\mathbf{B}$ projects the data into a one-dimensional subspace such that the between-group variability is maximum relative to within-group variability, and the associated eigenvalue λ_1 measures the ratio of the between-group and within-group variance. Analogous to PCA, the eigenvectors $\mathbf{e}_2, \mathbf{e}_3, \dots, \mathbf{e}_s$, $s \leq \min(p, k-1)$, where p is the number of wind speeds and k the number of clusters, project the data into subspaces such that the between-group variability is the 2nd, 3rd, \dots , s^{th} greatest relative to within-group variability (Krzanowski, 2001). The projections, or linear compounds, $\mathbf{e}_l^\top \mathbf{x}$ of the p -dimensional data points are termed the canonical variates (CVs). Note that, in the analysis of the firing rate data the $\min(5, 2) = 2$ and therefore, only two CVs exist; more details can be found in Krzanowski (2001).

Table 4 gives the coefficient vectors for the CVs, with the first producing the largest separation between groups as seen in Figure 4, which is also reflected in the λ_1 values being considerably larger than the λ_2 values in Table 5; this is similar to the PCA results where the first PC exhibited the largest separation between clusters (Figure 3). For the peri-stimulus period, the coefficients of the first CV predominately weigh on windspeeds 120 and 150, which is also similar to the PCA results. This is also evident in the similarity of Figures 4(a) and 3(a), which are both characterized by a large separation of neurons 9, 10, and 11 (blue group) from the rest. Compared to PCA, CVA yields a slightly better separation between neurons classified as low (red) and moderate (green) responders, likely a result of CVA maximizing the ratio of between-group variation to within-group variation.

Analogous to the results for the peri-stimulus period, the post-stimulus period shows a considerably larger first eigenvalue compared to the second, indicating that the first CV produces the largest segmentation of the neurons. The weights of the first two CVA coefficient vectors are similar to the PCA loadings, in that both methods place the largest weights on windspeeds 90 and 120. Furthermore, as CVA requires assignment of labels to the data points and the eigenvalues indicate the relative strength of the clustering structure, borderline data points can be manually shifted into alternate groups to assess the effects on the eigenvalues. Recall that in the k -means clustering results for the peri-stimulus data, neuron 32 was often assigned to the blue group instead of the green group depending on the initial centroids and therefore could be considered a borderline neuron. We perform CVA with neuron 32 manually redesignated to the high responder cluster (blue group), which resulted in the first two eigenvalues being 13.32 and 0.23. Figure 4(c) shows the plot with neuron 32 reclassified as a high responder. Comparing to Figure 4(a), we observe a similar separation between the red and green groups, but less separation for the blue group, which suggests that neuron 32 is best classified as a moderate responder (green group).

CVA Results Section 2.4 - Canonical Variate Loadings

	<u>1st CV</u>	<u>2nd CV</u>
Peri-stimulus	(0.156, -0.123, -0.034, 0.264, 0.302)	(0.0185, -0.054, 0.375, -0.170, 0.113)
Post-stimulus	(0.102, -0.057, 0.106, 0.567, 0.219)	(0.226, -0.331, 0.282, -0.178, 0.116)

Table 4: Loadings for the first two Canonical Variate Analysis Coefficient Vectors.

CVA Results Section 2.4 - Eigenvalues

	<u>1st Eigenvalue</u>	<u>2nd Eigenvalue</u>
Peri-stimulus	13.50	0.40
Post-stimulus	6.69	0.55

Table 5: Eigenvalues of $W^{-1}B$.

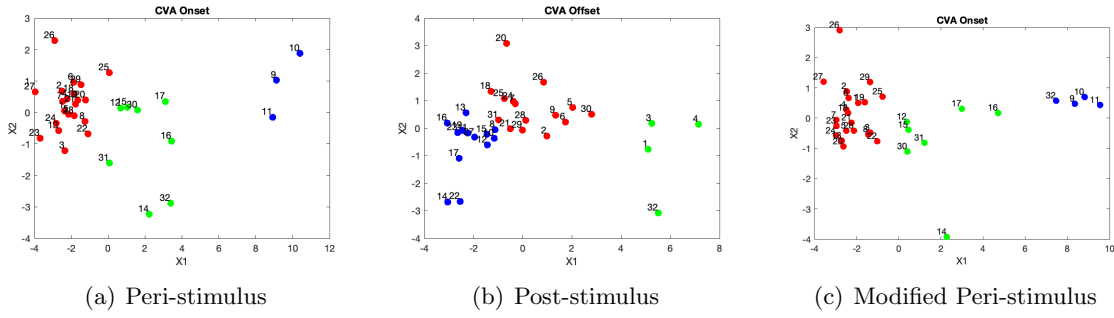


Figure 4: 1st vs. 2nd canonical variate plots for $k = 3$ clusters.

2.5 Summary

We see that employing the PCA and CVA methodologies yield nearly identical groupings, affirming the veracity and consistency of neuronal groupings thus defined. Since PCA is a more commonly employed and widely understood technique, in the ensuing explanation we utilize only the PCA results for interpretive purposes.

From Table 2, we see that the first principal component vector captures the majority of the variance in the data in both the peri-stimulus and post-stimulus clustering analyses; accordingly, Figure 3 shows that clusters arise primarily through variations in the first principal component vector. Furthermore, the Table 1 loadings show that wind speed 120 is the primary contributor to the variance in the first principal component vector, with wind speeds 90 and 150 contributing as well but less so, and wind speeds 30 and 60 contributing little. The lack of contribution of wind speeds 30 and 60 is intuitively clear – at these low wind speeds, with the lack of a potent stimulus, neurons tend to exhibit modest or vanishingly small responses, and hence response variability is small.

At the higher wind speeds – speeds 90, 120, 150 – neuronal responses tend to be more pronounced and hence capable of greater variability, allowing these wind speeds to provide greater contributions to the variance in the data. We might therefore expect that, for these three highest wind speeds, we should observe a trend of a progressively larger contribution to the variance in the data as wind speed is increased. Interestingly, such a trend is not apparent, as the largest contribution to the variance in the data comes from wind speed 120 (rather than wind speed 150); this is likely due to response saturation – i.e., at wind speed 150, many neurons likely tend to exhibit responses towards the upper end of the response spectrum, lowering response variability in comparison to wind speed 120, which likely tends to induce neuronal responses that are more evenly distributed throughout the full range of the response spectrum.

We can therefore conclude that a cluster on the right end of a plot in Figure 3 represents neurons that exhibit responses to wind speeds 90, 120, and 150 (but particularly wind speed 120) skewed towards the upper end of the response spectrum, in either the peri-stimulus or post-stimulus periods (Figure 3(a) and Figure 3(b), respectively). A cluster in the middle of a Figure 3 plot, then, represents neurons that exhibit modest responses to wind speeds 90, 120, and 150, while a cluster at the leftmost end represents neurons that exhibit little to no response to these wind speeds. Thus, with three apparent response types in the peri-stimulus period and three in the post-stimulus period, we expect a minimum of three and maximum of nine response types when the peri- and post-stimulus periods are conjoined. In other words, if we denote the high, modest, and low response types by A , B , and C , then the set of possible neuron types is $\{AA, AB, AC, BA, BB, BC, CA, CB, CC\}$, with the first letter denoting peri-stimulus and the second denoting post-stimulus response type.

While this clustering analysis provides a useful means to guide our intuition in relation to the types of neuronal response patterns that we can expect to observe, there are two important shortcomings to this approach. First, all wind speeds are necessarily combined and analyzed together, and hence information on the nature of a neuron’s response to any individual wind speed is not easily extracted, which precludes an investigation of the dependency of a neuron’s response type on wind speed.

Second, the methodology only analyzes time-averaged firing rates over a particular temporal epoch (the peri-stimulus or post-stimulus period), and therefore does not allow assessment of neuronal differences in response patterns throughout the temporal epoch in consideration – in particular, this implies that conjoining the peri- and post-stimulus periods into a single temporal epoch for analysis would discard all information on differences in neuronal responses across the two periods.

Thus, it is difficult, using this analysis, to entertain questions such as: Which of the above nine response types actually tend to occur? Can a neuron’s response type change with wind speed or is response type fixed for a given neuron across wind speeds? If a neuron’s response type can change with wind speed, are certain transitions likely to occur while others occur only rarely (e.g., perhaps *AC* neurons frequently transition into *CA* neurons as wind speed is increased but never transition into *AA* neurons)?. The answers to such questions require assessment of neuronal responses on a wind speed by wind speed basis, as well as a methodology that assesses response *patterns* (rather than simply time-averaged firing rates) throughout the temporal epoch in consideration (in particular, throughout the temporal epoch formed by conjoining the peri- and post-stimulus periods). We develop such a methodology in the following section.

3 Individual wind speed analysis

3.1 Introduction

The methods described above performed well at identifying the most significant groups when the responses are analyzed over all wind speeds together. However, of the three clusters, clusters 1 (red) and 2 (green), which contain the most observations, are not as clearly separated. Furthermore, it is possible that the response pattern of a fixed neuron may qualitatively vary at different wind speeds. That is, the methods in Sections 2 consider all five wind speeds in aggregate when performing a clustering analysis and therefore, cannot easily capture detailed changes in the response dynamics as a function of wind speed. We therefore propose another method that compares response patterns between neurons by analyzing the firing rate as a function of time over the entire recording epoch, and then perform a cluster analysis based on the dissimilarity between the neurons at each individual wind speed. Our goal here is to analyze the neural response curve as a whole over the entire peri- and post-stimulus intervals at each wind speed. That is, instead of taking the average firing rate over the peri-stimulus/post-stimulus period, we consider each observed response as a curve and utilize a metric for comparison that effectively captures the dissimilarity of shape differences between responses.

3.2 Hausdorff distance methodology

There are many methods to quantify the similarity, or dissimilarity, between two response curves. Two popular procedures are Dynamic Time Warping (DTW) and Canonical Time Warping (CTW); see Sakoe and Chiba (1978) and Zhou and Torre (2009). However, the drawbacks of these alignment-based methods in this specific study is that they do not perform well in comparing patterns between curves when the firing rate peaks have different time offsets. As shown in Figure 5, Dynamic Time

Warping shifts the two different response curves to a common interval that aligns the peaks prior to obtaining a measure of dissimilarity. In the top panel, the orange signal is a peri-stimulus responder with the highest peak value in the interval 0 – 10ms, while the blue curve, a post-stimulus responder, peaks in the interval 17 – 30ms. In the bottom panel of Figure 5, the DTW algorithm aligns the two curves so that the peaks match as close as possible. Therefore, this type of method is not suitable to the goals of this study, since, for example, such an algorithm may estimate the same degree of similarity between a peri-stimulus and post-stimulus responder versus two peri-stimulus responders.

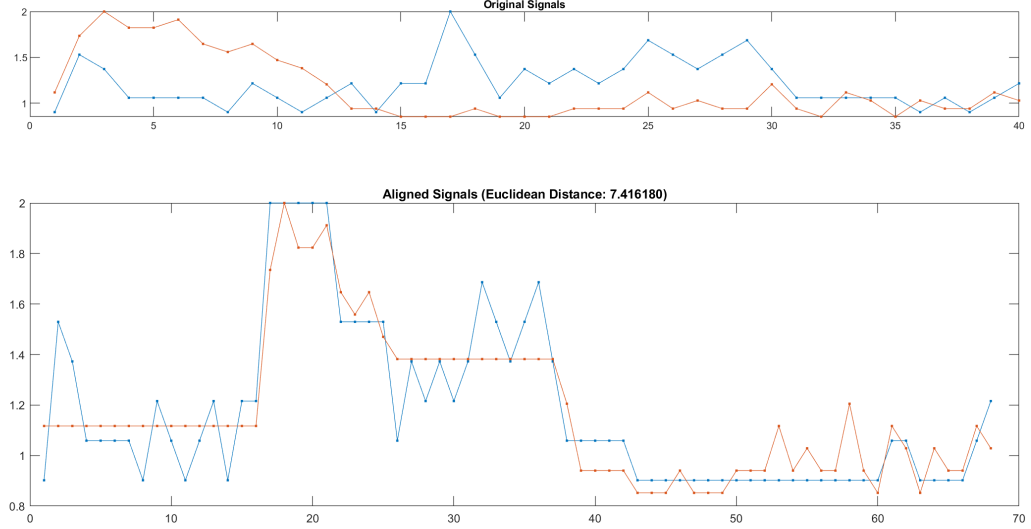


Figure 5: Example of Dynamic Time Warping to measure the similarity between two neuronal response curves. In the top panel, two neural activities are shown as line plots. The orange signal peaks in the region of time steps 5-10ms, while the blue signal peaks in 17-30ms. However, the aligned signals from the bottom panel shows that the two signals are aligned together, which is not desired.

Instead of the previously discussed methods, we propose the Hausdorff distance as a measure of the dissimilarity between neuronal response curves. In Euclidean space, the smallest distance between a point a and a set of points B is naturally given as

$$\tilde{d}(a, B) = \inf_{b \in B} d(a, b).$$

Note that, $\sup_{a \in A} \tilde{d}(a, B)$ is then interpreted as the largest shortest distance from a set of points A to B . The Hausdorff distance between A and B is then defined as

$$d_H(A, B) = \max\{\sup_{a \in A} \tilde{d}(a, B), \sup_{b \in B} \tilde{d}(A, b)\}, \quad (3.1)$$

which is the maximum of the largest shortest distance from A to B or from B to A . In this study,

the sets A and B are the firing rates observed over the entire recording epoch for the two neuronal response curves being compared. This method accounts for the temporal differences between the peaks of the compared response patterns, which addresses the short-falls of methods such as DTW.

3.3 Smoothed data

The definition of the Hausdorff distance suggests that it can be sensitive to extreme values or noisy data and as a result, can be dominated by unusual observations. We therefore perform variance reduction on the sequential spike count data using the LOWESS (Locally Weighted Scatterplot Smoothing) kernel smoothing technique. Figure 6 shows the data smoothed using three different bandwidths. The results in Figure 6 (b) show that an overly low bandwidth results in overfitting, an overly high bandwidth, Figure 6 (c), results in underfitting, while the bandwidth 0.35 used in Figure 6 (a) captures the general trend in firing rate while minimizing large fluctuations that are likely due to trial-to-trial noise. We determined the ideal smoothing based on visual inspection together with consideration of the biological plausibility. While other methods that do not require hyperparameter tuning such as penalized splines could have been employed, our approach proved effective and the clustering results were accurate in practice.

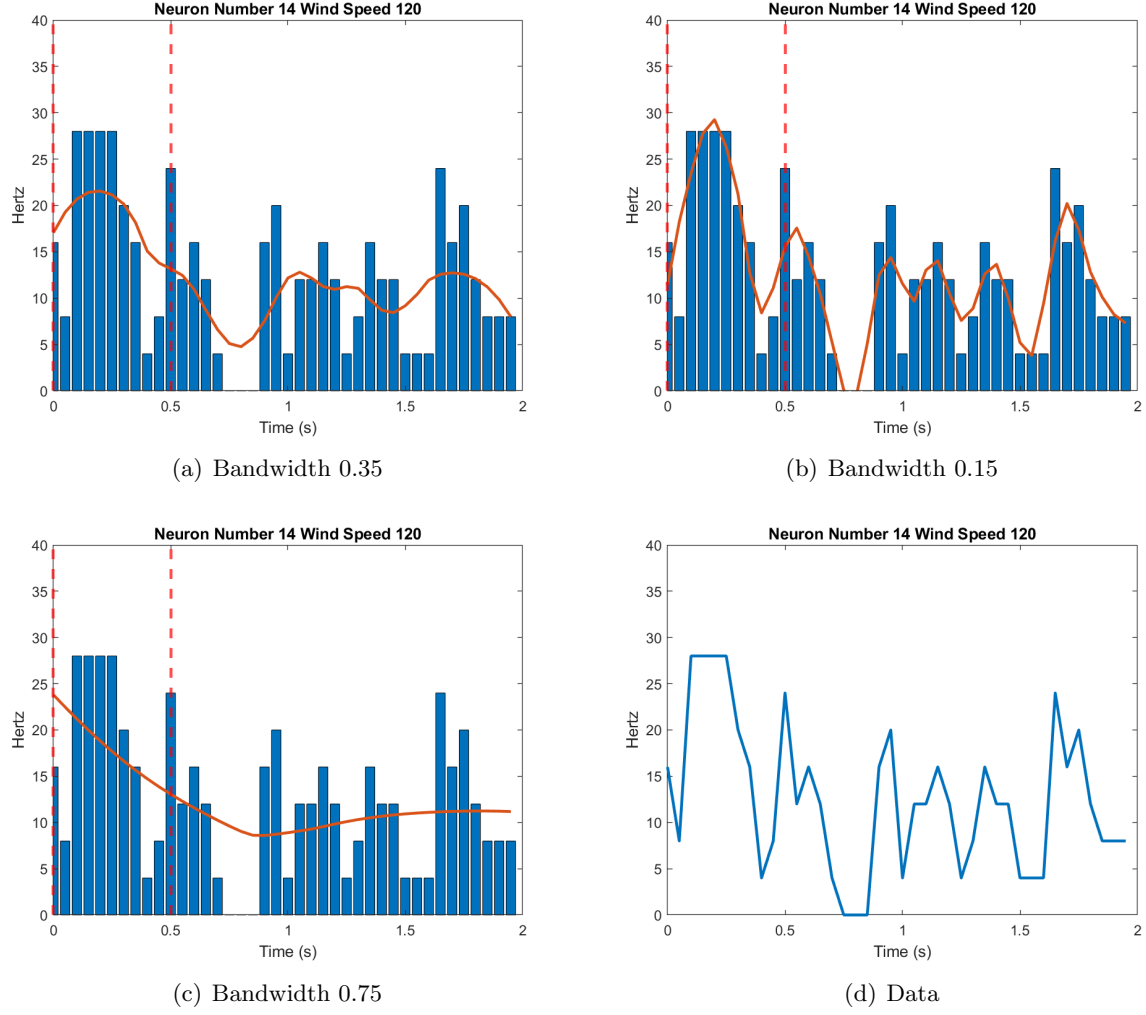


Figure 6: Example of the kernel smoothing method LOWESS to reduce noise in the response activity of the neurons. The LOWESS method requires a hyperparameter - span (bandwidth), which denotes the fraction of data to use with the fitting procedure. Panel (a), (b), (c) shows a fit of the curve using a span of 0.35, 0.15, and 0.75 respectively. Panel (d) shows a graph without smoothing.

3.4 Hausdorff distance based cluster analysis

Different from the analysis performed in Section 2, we calculated the Hausdorff distances between all pairs of LOWESS smoothed neuronal response curves, measured over the conjoined peri and post-stimulus periods, at each wind speed; these distances produce a dissimilarity matrix, which can be visualized as a heatmap. For example, Figure 7 shows the heatmap for wind speed 120; we observe the existence of one outlying neuron (13) - this neuron is considered its own individual group in the subsequent cluster analysis. That is, the clustering analysis is performed on the data with this neuron omitted. Additionally, two outlying neurons (14, 22) were identified at wind speed 90, and one outlying neuron (27) at wind speed 150, and these neurons were treated analogously.

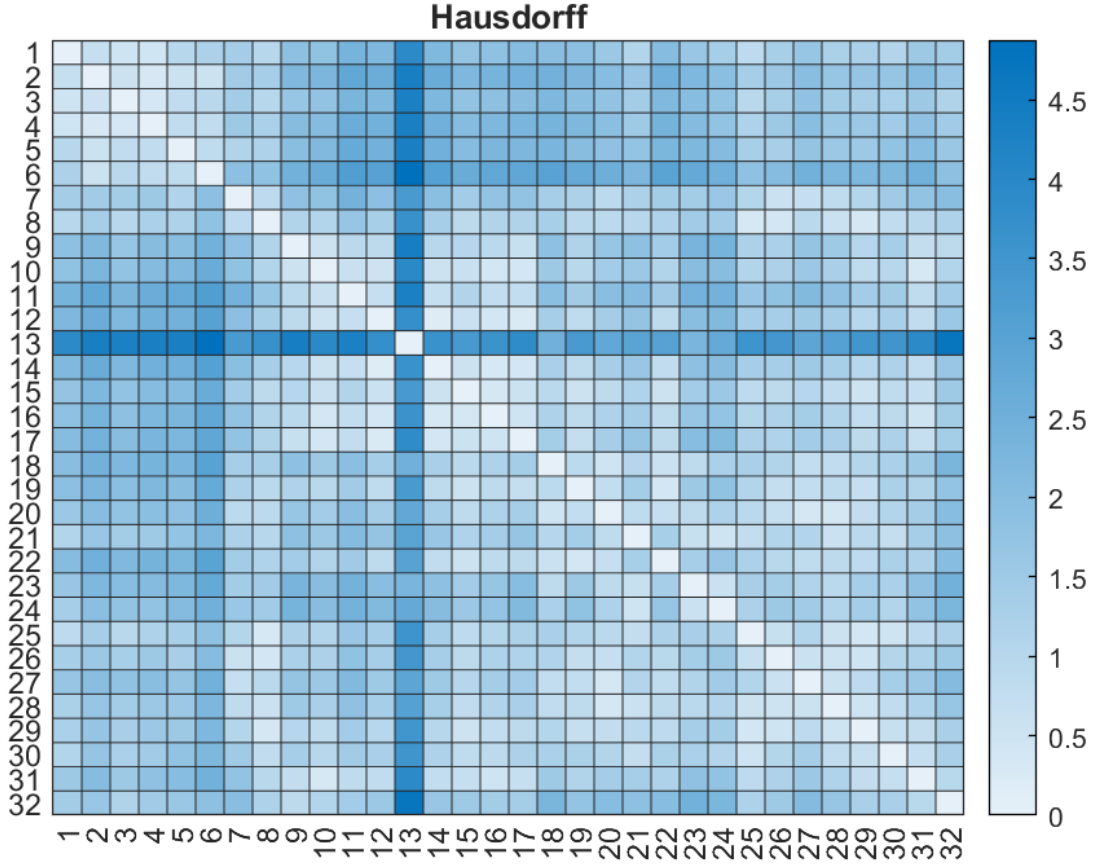


Figure 7: Hausdorff pairwise distances at wind speed 120.

Since the individual neuronal responses are measured as multiple observations over time, we cannot apply k -means clustering as it relies on single-valued observations. Instead, we employ the hierarchical clustering method Agglomerative Nesting (AGNES) using the complete linkage function. An advantage of the AGNES method is that the number of clusters k does not need to be specified and only requires that a dissimilarity measure, or distance, has initially been calculated between each pair of the n observations. In the first stage of the nesting procedure, each observation is considered as an individual cluster and the two objects with the smallest dissimilarity are joined to form one cluster, and then at each subsequent step the two nearest clusters, which can contain one or any number of observations, are merged to form, or enlarge, the cluster. The process is continued until all observations are merged into one final cluster that contains all observations. For the AGNES algorithm we chose the *farthest neighbor method*, or the complete linkage function, originally defined in Sokal and Michener (1958). Specifically, consider two clusters A and B , let $d(a, b)$ be the dissimilarity measure between any two observations (a, b) and, as in Lance and Williams

(1966b), define the distance between the clusters as

$$D(A, B) = \max_{a \in A, b \in B} d(a, b), \quad (3.2)$$

with $d(A, A)$ defined to be 0. Note that, in our analysis the dissimilarity measure $d(i, j)$ is the Hausdorff distance (3.1) between the neural response curves of neuron i and j , respectively. In the l^{th} step, $1 < l < n$, of the agglomerative nesting procedure a new dissimilarity matrix of dimension $n - l$ is determined that provides the pairwise distances between each of the remaining clusters using (3.2). We opted to use the complete linkage function for the following reasons: 1. The complete linkage method yielded the highest agglomerative coefficient across all wind speeds, producing the best empirical performance; 2. The method of the shortest farthest distance is similar in spirit to the Hausdorff distance, as it measures the largest dissimilarity between two clusters. Note that, the agglomerative coefficient (AC), a measure between 0 and 1, provides a measure of the quality of the segmentation, or the overall quality of the clustering structure, achieved by the farthest neighbor link function. An AC value closer to 1 typically implies that a strong clustering structure has been recovered.

The AGNES clustering method, using the Hausdorff distance based dissimilarity measure, was implemented to identify differences in the neuronal response curves at each wind speed, with dendrograms produced to visualize the segmentation of the observations at each stage of the agglomerative process. A dendrogram, or tree diagram, is a graphical illustration of the agglomerative nesting procedure where the vertical axis gives the dissimilarity values between the merged clusters at each step; see Kaufman and Rousseeuw (1990) or Everitt et. al (2001) for more details. To determine the number of clusters, or the cutoff in the agglomeration, we find the step that increases dissimilarity the most when merging clusters, and obtain the clusters that are formed by the previous merge; this corresponds to finding the longest lines between nodes in the dendrogram. The dendrogram for wind speed 120 is shown in Figure 8, with histograms for a single neuron from each cluster, including the outlying neuron (13), shown in Figure 9. For this wind speed, there are three clusters - note that this is consistent with the results of the k -means cluster analysis in Section 2.2. Also, the AC is 0.77, and together with the distinct clustering structure in the dendrogram in Figure 8, with neuron (13) considered as its own group, supports the segmentation of the neurons into $k = 3$ clusters. Note that the cluster in the far left of the dendrogram corresponds to the post-stimulus responders, and the group on the far right corresponds to the peri-stimulus responders. Furthermore, on investigating the relative firing rate histograms of the neurons, the middle group of neurons were identified as low responders, meaning that they have a moderate response at this wind speed.

For wind speed 90, segmentation into three groups results in a random partition of the peri-stimulus group and thus, the neurons are only divided into two groups, peri-stimulus and post-stimulus responders. When the wind speed increases to 120 and 150, the peri-stimulus group divides into strong peri-stimulus responders and mild peri-stimulus responders. An analogous analysis of the two lowest wind speeds did not result in a strong clustering structure. At the two lowest wind

speeds, neurons were mostly unresponsive and exhibited only background firing rates throughout the recording period. Even implementing the cutoff from the dendrograms at the largest distance between nodes did not produce meaningful clusters. Therefore, we conclude that there are no distinct classifications of the neuronal responses at these lower wind speeds.

Interestingly, it was observed that group identification of a neuron can change with wind speed. In other words, a neuron can, for example, shift from a strong peri-stimulus responder to a post stimulus responder with changing wind speed. In order to quantify the trends of transitions in group identification for changing wind speeds, Figure 10 shows the empirical transition probabilities among groups across the three highest wind speeds. For example, stim-on neurons (peris-stimulus responders) at wind speed 90 split into strong stim-on neurons and mild stim-on neurons at wind speed 120, with a 0.5 relative frequency of a neuron transitioning to either group.

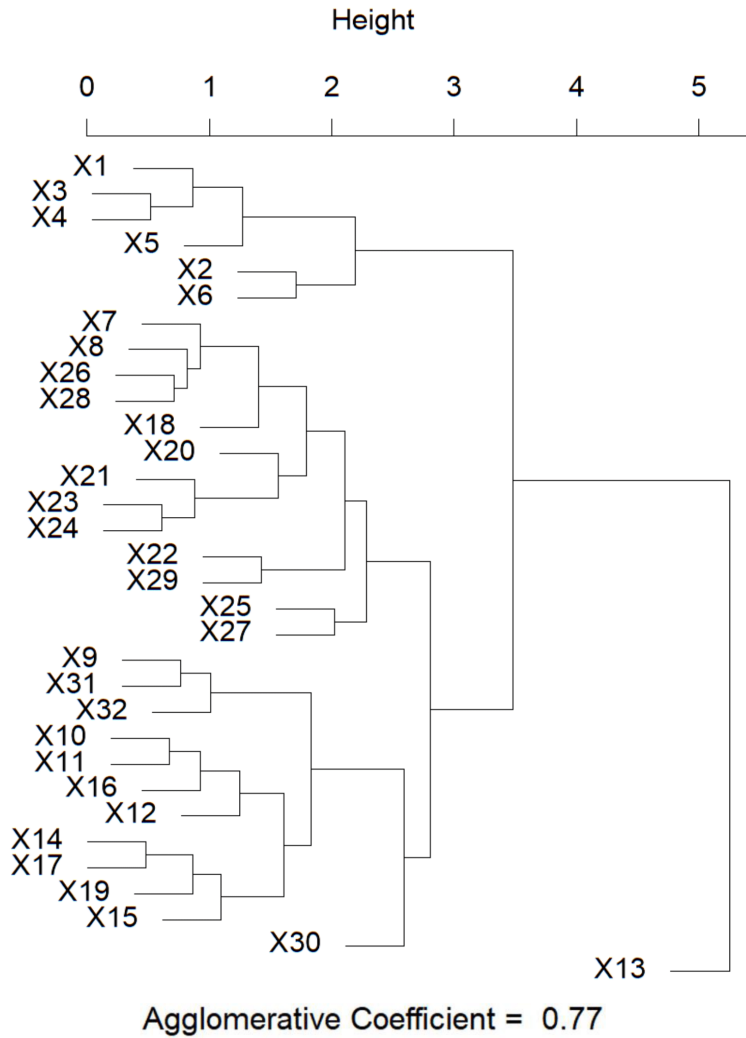


Figure 8: Dendrogram wind speed 120.

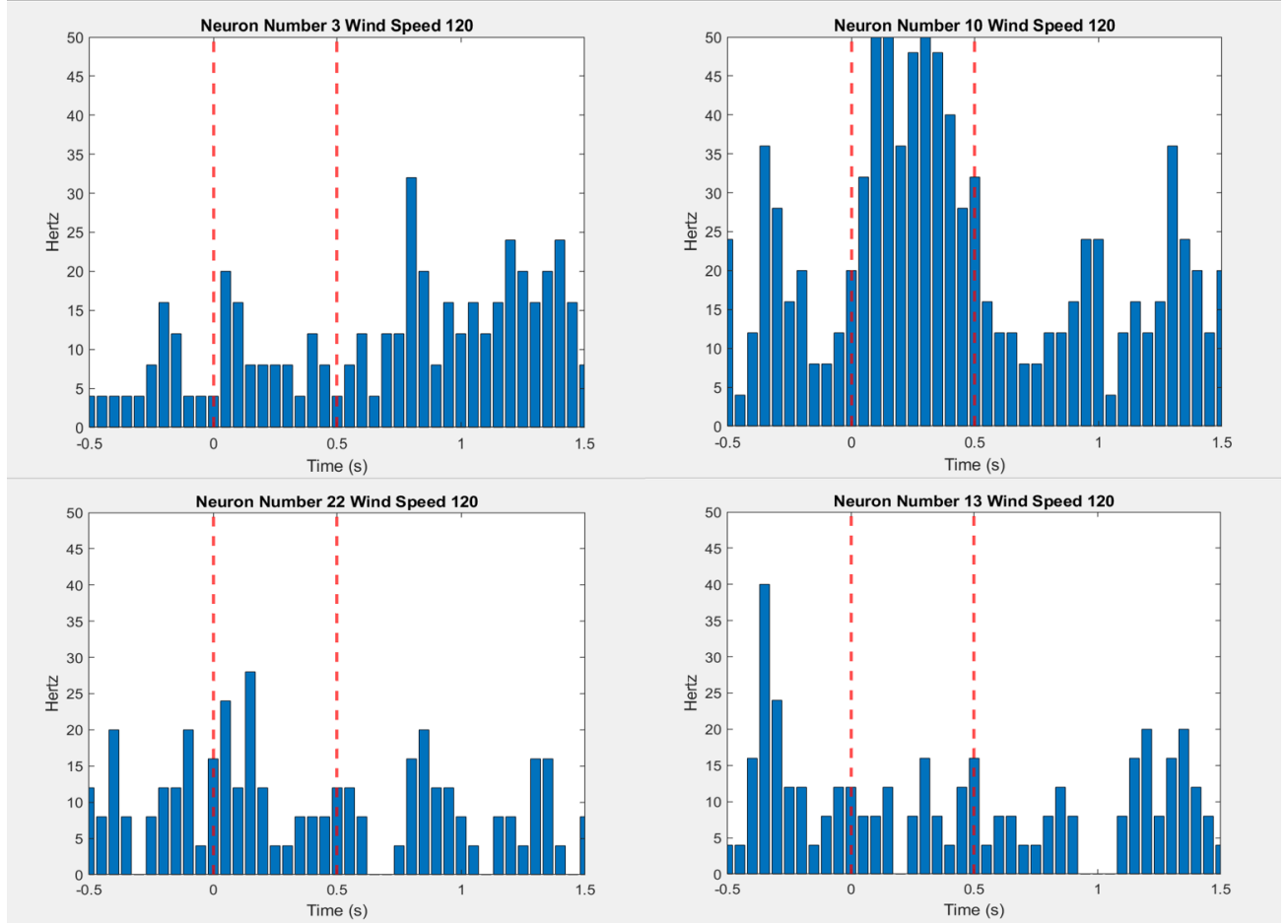


Figure 9: Bar plots of neurons exhibiting different responding patterns. The x-axis shows time in seconds, and the y-axis shows firing rate in Hertz. The two dotted red lines represent the onset and offset of stimulus. 1(a) is a strong post-stimulus responding neuron, 1(b) is a neuron responding during the stimulus, 1(c) is a neuron that tends to have a delayed response, and 1(d) is a non-responder which exhibits activity no different than background during the stimulus..

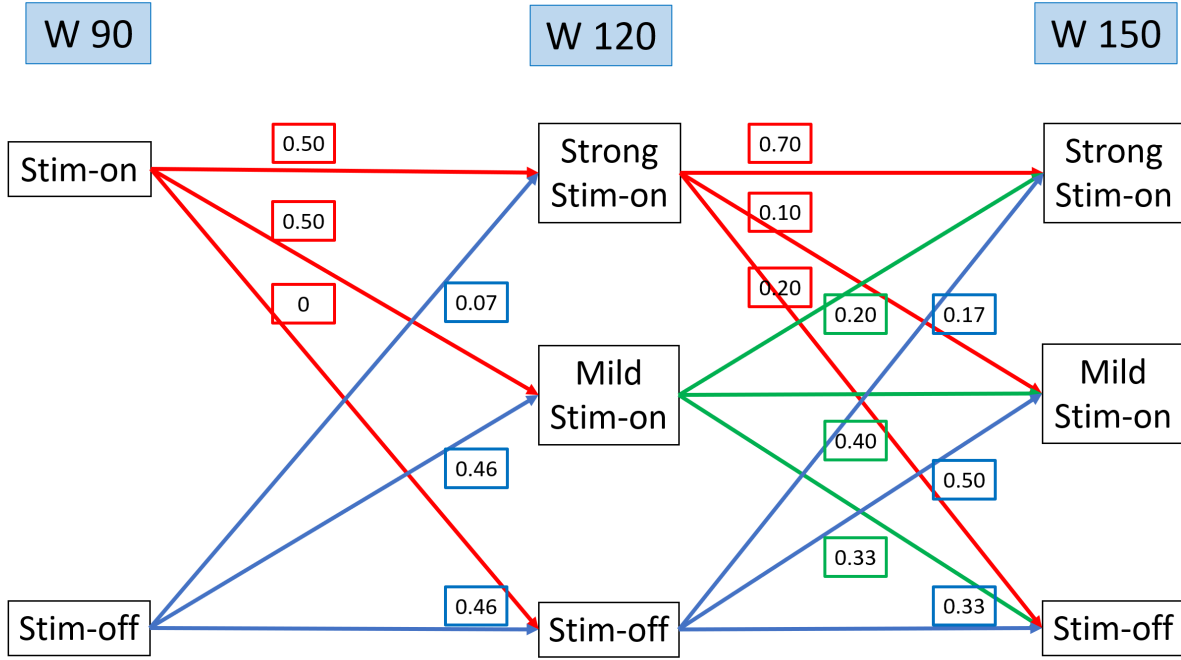


Figure 10: Graph illustrating the relative transition frequencies among the three response groups across the top three wind speeds. Each arrow color represent neurons transitioning from the same group.

3.5 Summary

The methodology described above clusters neurons based on similarities and differences in spiking *patterns* (rather than coarse-grained time-averaged firing rates) over the temporal epoch in consideration, allowing the peri- and post-stimulus periods to be conjoined into a single temporal epoch and clustering based on detailed differences in spiking patterns across this entire temporal epoch. Moreover, this methodology allows clustering on a wind speed by wind speed basis, permitting us to ascertain the dependency of neuronal spiking patterns on wind speed.

Figure 10 shows, interestingly, that neuronal spiking patterns in response to mechanosensory input are not fixed, but rather are dependent on stimulus intensity. At the two lowest wind speeds (results not shown), no clusters emerge from the analysis, likely due to responses at these low stimulus intensities being small to nonexistent and hence lacking appreciable distinction from neuron to neuron. At wind speed 90, only two clusters emerge – neurons that respond during the peri-stimulus period (stim-on) and those that respond during the post-stimulus period (stim-off). As wind speed is increased to 120, and neuronal responses become larger, greater distinctions between neuronal spiking patterns become apparent and the methodology detects the emergence of a third cluster. The stim-on neurons from wind speed 90 split into two groups at wind speed 120 – those that respond mildly (mild stim-on) and those that respond strongly (strong stim-on) during the peri-stimulus period; stim-off neurons from wind speed 90 tend to either remain stim-off or, interestingly, become

mild stim-on neurons. From wind speed 120 to 150, we see that response types can change even more drastically – any of the three response types is capable of remaining the same or transitioning into either one of the other two.

4 Discussion

In this work, we develop a statistical methodology for algorithmically separating and classifying neuronal spiking patterns. The methodology involves two broad steps: (1) k -means clustering, using time-averaged firing rates, over subintervals of the relevant response period based on data aggregated over stimuli, which allows inference of the types of stimulus-induced neuronal response patterns that can be expected; (2) Analysis informed by the results of the prior step, that classifies and clusters neuronal response patterns over the entire relevant response period on a stimulus-by-stimulus basis. While we demonstrate this methodology on a data set of stimulus-induced spiking patterns of AL neurons, this procedure can be applied to a broad array of data sets where separation and classification of distinct neuronal spiking patterns is desired.

The methodology described in this work, applied to our novel data set of responses of AL neurons to mechanosensory input of varying wind speed, yields a striking physiological result that, to our knowledge, has not previously been observed or studied within the literature – namely, that the response pattern of an AL neuron to mechanosensory input can change dramatically with stimulus intensity. While the physiological mechanisms underlying this phenomenon cannot be ascertained from this work, several possibilities in general exist: (i) the phenomenon occurs at the level of peripheral mechanosensory receptors, and response patterns are simply inherited by AL neurons from these peripheral receptors; (ii) response patterns at the periphery do not qualitatively change with wind speed, and response patterns at the level of the AL change due to intrinsic network mechanisms; (iii) both changes in peripheral response patterns and intrinsic network mechanisms within the AL contribute to the phenomenon.

Possibility (i) is not as intriguing from the perspective of the AL, since the implication is that qualitatively striking shifts in response patterns within the AL are simply inherited from the input. Possibility (ii), however, implies a far more intriguing view of the AL; possibility (ii) suggests that as wind speed is increased the mechanosensory input to an AL neuron, for example, simply increases the intensity of its stim-on spiking pattern while the response of the AL neuron transitions from a stim-on to a stim-off spiking pattern. Such a phenomenon would need to be explained by dynamical mechanisms internal to the AL, with potential explanations including a differential effect of increasing wind speed on the input to excitatory projection neurons (PNs) versus inhibitory local neurons (LNs) within the AL, activation of a potent slow inhibitory current permeating the AL network beyond a certain threshold as stimulus intensity rises, or dynamical consequences resulting from a more global versus focal stimulation of the AL network as wind speed is increased. This list of potential explanations, of course, is not exhaustive, and further investigations are needed to elucidate the physiological and dynamical underpinnings of this phenomenon.

Furthermore, there may be another mechanism, in addition to direct mechanosensory input from the periphery, through which mechanosensory dynamics at the antennae may modulate AL responses – a mechanism based on biophysical changes of the boundary layer on the surface of the antennae. When air flows across a rigid surface, the velocity drastically decreases when getting closer to the hard surface, thus forming a boundary layer [36]. The spatial distribution of various types of sensilla, especially the hair-like sensilla, on the antennal surface facilitates the formation of this layer. Odor molecules are arrested at the top of the boundary layer first before diffusing into the pores of olfactory sensilla. The thickness of the boundary layer therefore affects how the odor molecules are received by the sensory neurons [28]. This is especially the case in honey bee antenna because most of the olfactory sensilla (pore plates) are disk-like structures on the surface [26]. When air speed increases, the boundary layer becomes thinner, resulting in faster odor diffusion [18], allowing air speed dynamics to impact AL odor responses via a mechanism independent of the direct mechanosensory input to the AL described in this paper.

Thus, there is likely a complex interplay of mechanosensory input with olfactory input within the AL through multiple mechanisms. A comprehensive understanding of the physiological and functional significance of this phenomenon therefore requires study of both direct and indirect impacts of mechanical sensation at the periphery on the input to the AL as well as the internal dynamics of the AL and how such dynamics sculpt AL responses in a continuously changing mechanosensory and olfactory environment. Systematic characterization of AL responses to pure mechanosensory input, as carried out in this paper, provides a necessary first step in such an endeavor.

References

- [1] B. Ache and J. Young. Olfaction: Diverse species, conserved principles. *Neuron*, 48:417–430, 2005.
- [2] K. Baker, G. Vasan, A. Gumaste, V. Pieribone, and J. Verhagen. Spatiotemporal dynamics of odor responses in the lateral and dorsal olfactory bulb. *PLoS Biology*, 17:e3000409, 2019.
- [3] J. Boeckh, K.D., and H. Polz. Convergence of inputs from different sense organs upon neurones of the central antennal pathway in insects. convergence of inputs from different sense organs upon neurones of the central antennal pathway in insects. *E Horn*, Stuttgart New York, Gustav Fischer:143–148, 1983.
- [4] A. Brinkmann and D. Schild. One special glomerulus in the olfactory bulb of xenopus laevis tadpoles integrates a broad range of amino acids and mechanical stimuli. *J Neurosci*, 36:10978–10989, 2016.
- [5] R. Carde and M.. Willis. Navigational strategies used by insects to find distant, wind-borne sources of odor. *J Chem Ecol*, 34:854–866, 2008.

- [6] A. Froese, P. Szyszka, and R. Menzel. Effect of gabaergic inhibition on odorant concentration coding in mushroom body intrinsic neurons of the honeybee. *J Comp Physiol*, 200:183–195, 2014.
- [7] C. Galizia and R. Vetter. Optical methods for analyzing odor-evoked activity in the insect brain. *Advances in Insect Sensory Neuroscience*, CRC Press: Boca Raton:349–392, 2004.
- [8] C. et al. Gray. Tetrodes markedly improve the reliability and yield of multiple single-unit isolation from multi-unit recordings in cat striate cortex. *Journal of Neuroscience Methods*, 63:43–54, 1995.
- [9] Q. Han, B. Hansson, and S. Anton. Interactions of mechanical stimuli and sex pheromone information in antennal lobe neurons of a male moth, *spodoptera littoralis*. *J Comp Physiol A Neuroethol Sens Neural Behav Physiol.*, 191:521–528, 2005.
- [10] R. Iwata, H. Kiyonari, and T. Imai. Mechanosensory-based phase coding of odor identity in the olfactory bulb. *Neuron*, 96:1139–1152, 2017.
- [11] A. Jarman. Studies of mechanosensation using the fly. *Human Mol Gen*, 11:1215–1218, 2002.
- [12] J. Joerges, A. Kuttner, G. Galizia, and R. Menzel. Representations of odours and odour mixtures visualized in the honeybee brain. *Nature*, 387:285–288, 1997.
- [13] R. Kanzaki, E. Arbas, N. Strausfeld, and J. Hildebrand. Physiology and morphology of projection neurons in the antennal lobe of the male moth *manduca sexta*. *J Comp Physiol A*, 165:427–453, 1989.
- [14] J. Lee and N. Strausfeld. Structure, distribution and number of surface sensilla and their receptor cells on the olfactory appendage of the male moth *manduca sexta*. *J Neurocytol*, 19:519–538, 1990.
- [15] H. Lei, T. Christensen, and J. Hildebrand. Spatial and temporal organization of ensemble representations for different odor classes in the moth antennal lobe. *J Neurosci*, 24:11108–11119, 2004.
- [16] B. Malnic, J. Hirono, T. Sato, and L. Buck. Combinatorial receptor codes for odors. *Cell*, 96:713–723, 1999.
- [17] A. Mamiya and M. Dickinson. Antennal mechanosensory neurons mediate wing motor reflexes in flying *drosophila*. *J Neurosci.*, 35:7977–7991, 2015.
- [18] M. Moore, K. Weighman, A. Steele, B. Cordova, and P. Moore. Comparative analysis of the boundary layer filtering of odor signals in the amblypygid (whip spider) species *paraphrynus laevifrons* and *phrynus marginemaculatus*. *Journal of Insect Physiology*, 120:103984, 2020.

- [19] J. Murlis, J. Elkinton, and R. Carde. Odor plumes and how insects use them. *Ann Rev Entomol*, 37:505–532, 1992.
- [20] J. Murlis and C. Jones. Fine-scale structure of odor plumes in relation to insect orientation to distant pheromone and other attractant sources. *Physio Ento*, 6:71–86, 1981.
- [21] M. Ng, R. Roorda, S. Lima, B. Zemelman, P. Morcillo, and G. Miesenbock. Transmission of olfactory information between three populations of neurons in the antennal lobe of the fly. *Neuron*, 36:463–474, 2002.
- [22] M. Patel, N. Kulkarni, H. Lei, K. Lai, O. Nematova, K. Wei, and H. Lei. Experimental and theoretical probe on mechano- and chemosensory integration in the insect antennal lobe. *Frontiers in Physiology*, 13:1004124, 2022.
- [23] M. Patel and A. Rangan. Olfactory encoding within the insect antennal lobe: The emergence and role of higher order temporal correlations in the dynamics of antennal lobe spiking activity. *J Theor Biol*, 522:110700, 2021.
- [24] M. Patel, AV. Rangan, and D. Cai. A large-scale model of the locust antennal lobe. *J of Comput Neurosci*, 27(3):553–567, 2009.
- [25] M. Patel, A.V. Rangan, and D. Cai. Coding of odors by temporal binding within a model network of the locust antennal lobe. *Frontiers Comput Neurosci*, 7:1–18, 2013.
- [26] A. Riveros and W. Gronenberg. Sensory allometry, foraging task specialization and resource exploitation in honeybees. *Behavioral Ecology and Sociobiology*, 64:955–966, 2010.
- [27] S. Sane, A. Dieudonne, M. Willis, and T. Daniel. Antennal mechanosensors mediate flight control in moths. *Science*, 315:863–866, 2007.
- [28] R. Schneider, J. Lanzen, and P. Moore. Boundary-layer effect on chemical signal movement near the antennae of the sphinx moth, *manduca sexta*: temporal filters for olfaction. *Journal of Comparative Physiology A-Sensory Neural and Behavioral Physiology*, 182:287–298, 1998.
- [29] M. Strube-Bloss, M. Herrera-Valdez, and B. Smith. Ensemble response in mushroom body output neurons of the honey bee outpaces spatiotemporal odor processing two synapses earlier in the antennal lobe. *PLoS One*, 7:e50322, 2012.
- [30] E. Tiraboschi, L. Leonardelli, G. Segata, and A. Haase. Parallel processing of olfactory and mechanosensory information in the honey bee antennal lobe. *Frontiers in Physiology*, 12:790453, 2021.
- [31] H. Tuckman, J. Kim, A. Rangan, H. Lei, and M. Patel. Dynamics of sensory integration of olfactory and mechanical stimuli within the response patterns of moth antennal lobe neurons. *Journal of Theoretical Biology*, 509:110510, 2021.

- [32] H. Tuckman, M. Patel, and H. Lei. Effects of mechanosensory input on the tracking of pulsatile odor stimuli by moth antennal lobe neurons. *Frontiers in Neuroscience*, 15:739730, 2021.
- [33] N. Vickers. Mechanisms of animal navigation in odor plumes. *Biol Bull*, 198:203–212, 2000.
- [34] N. Vickers and T. Christensen. A combinatorial model of odor discrimination using a small array of contiguous, chemically defined glomeruli. *Ann NY Acad Sci*, 855:514–516, 1998.
- [35] N. Vickers, T. Christensen, and J. Hildebrand. Combinatorial odor discrimination in the brain: Attractive and antagonistic odor blends are represented in distinct combinations of uniquely identifiable glomeruli. *J Comp Neurol*, 400:35–36, 1998.
- [36] S. Vogel. Life in moving fluids: The physical biology of flow - revised and expanded second edition. *Princeton University Press*, 1994.
- [37] U. Walldow. Multimodale neuron im deutocerebrum von periplaneta americana. *Journal of Comparative Physiology*, 101:13, 1975.
- [38] J. Wang, A. Wong, J. Flores, L. Vosshall, and R. Axel. Two-photon calcium imaging reveals an odor-evoked map of activity in the fly brain. *Cell*, 112:271–282, 2003.
- [39] A. Whitehead and J. Larsen. Ultrastructure of the contact chemoreceptors of apis mellifera l. (hymenoptera : Apidae). *Int J Insect Morphol Embryol*, 5:301–315, 1976.
- [40] R. Zeiner and H. Tichy. Combined effects of olfactory and mechanical inputs in antennal lobe neurons of the cockroach. *J Comp Physiol A*, 182:467–473, 1998.